13C tracer deposition in EAST D and He plasmas investigated by high-throughput deuteron nuclear reaction analysis mapping

S. Möller [a,*], R. Ding [b,*], H. Xie [b], B.F. Gao [b,c], B.G. Wang [b,c], J. Peng [a,b], S.C. Liu [b], W. Gao [b], A. Kirschner [a], U. Breuer [d], P. Wienhold [a], R. Krug [a], S. Brezinsek [a]

[a] Forschungszentrum Jülich GmbH, Institut für Energie- und Klimaforschung, 52425 Jülich, Germany
[b] Institute of Plasma Physics, Chinese Academy of Sciences, Hefei, Anhui 230031, China
[c] University of Science and Technology of China, Hefei 230026, Anhui, China
[d] Forschungszentrum Jülich GmbH, Zentralinstitut für Analytik, 52425 Jülich, Germany

ARTICLE INFO

ABSTRACT

Rare isotope tracer injection represents an established way for following particle transport in fusion research, but a tracer experiment is only as good as the tracer can be followed and separated from the common isotope. Physical models for transport analysis such as ERO2.0 require accurate total amounts of deposition with high spatial resolution. This work describes an extended high throughput NRA post analysis approach together with the surface analysis results of 2 technically rough graphite-tiles of 150x150 mm^2 surface area exposed to D and He plasmas in EAST.

The applied 1.43 MeV deuteron beam NRA offers percent range accuracy for layer thicknesses ranging from few 10 nm to 20 μm. Optimisation of the beam line and beam optics enables operation with ≤20 nA without reaching critical radiation levels, resulting in a measurement time of 5–10 s per spot. This enabled acquiring in total 3070 NRA points on the central 46×46 mm^2 cut-outs of each sample and an adjacent part of equal size within 12 h of analysis time.

The layers contained 50–60% D, ~2% ^{12}C, and ~3% O. The central 20 mm radius around the injection hole contains 98% of the total ^{13}C deposition. NRA finds up to $5.8 \pm 0.9 \times 10^{22}$ $^{13}C/m^2$ close to the hole with an e-folding fall-off length of about 3–10 mm in every radial direction. In the D discharge $24 \pm 2\%$ and $16 \pm 2\%$ in He of the injected ^{13}C are found on the tiles with triangle shaped deposition profiles following ExB. The comparison to colour fringe analysis and SIMS reveals the particular strength of D-NRA regarding roughness, thick layers, and the separation of ^{12}C and ^{13}C deposits, but in compatible regions all methods agree. Compared to these, the NRA yields additional information indicating depositing species and physical processes.

1. Introduction

Fusion research uses rare isotope tracers for separation of plasma-surface interaction (PSI) and plasma edge transport of different elements such as nitrogen, carbon or beryllium. In particular devices with carbon based plasma-facing components (PFC) make use of ^{13}C labelled methane for PSI and edge plasma physics studies. These studies have a long history in numerous fusion devices such as TEXTOR [1], ASDEX Upgrade [2], JET [3], and DIII-D [4]. Typically, these studies inject a known amount of ^{13}C-methane via mm sized injection holes at a specific location inside the plasma vacuum vessel. Spectroscopy based diagnostics follow the injected particles in-situ via their light emission in

the plasma. Post-mortem analysis of PFCs or parts of them enables quantification of the deposited amount and its local distribution. In particular in combination with PSI models such as ERO [5], tracer studies enable deepening of the physical understanding of transport and erosion in fusion reactors.

The studies demonstrated local deposition efficiencies in the order of 0.1 to 30% of the injected ^{13}C atoms, depending on the experimental conditions like spatial scope of the investigation, the plasma parameters, or the target properties. Numerous physical and chemical processes at the plasma edge reform the injected ^{13}C bound in molecular form (CH_4) to carbon and numerous hydrocarbon species, all with different properties of transport and surface sticking. At the same time the removal by

sputtering competes with the deposition by sticking, resulting in a certain net quantity accessible for post-mortem analysis. The deposition efficiency, i.e. the number of deposited ^{13}C within the area of interest relative to the number of injected ^{13}C, was seen to increase with surface roughness, since this lowers sputtering and increases sticking. This makes experiments with rough target surfaces less reproducible compared to polished surfaces, but the technical reality of fusion devices requires using technically rough surfaces for representative results. ERO modelling investigating the processes required a so-called enhanced re-erosion coefficient >1 [6,7]. This coefficient represents the factor of increased sputtering yield of freshly formed co-deposits, but its origin was not completely understood, so far. In conclusion, several open questions of technological and physical origin remain open to be solved by future tracer studies.

A tracer experiment is only as good as the tracer can be followed and separated from the common isotope, e.g. ^{13}C vs. ^{12}C. A detailed comparison to models requires accurate total amounts (deposition efficiency) and highly resolved spatial distributions. The aforementioned studies conducted this post-analysis by Proton Rutherford-Backscattering spectrometry (RBS), ^{3}He Nuclear reaction analysis (NRA), Secondary ion mass spectrometry (SIMS), or interference colour fringe analysis or a combination of those. NRA and RBS offer a particularly good solution for localising tracer isotopes due to their nuclear sensitivity, low detection limits, and insensitivity of absolute quantification to surface roughness [8], but they are limited to rather thin layers and only limited lateral sample coverage. Colour fringe analysis remains limited to transparent layers, which means typically <1 μm thickness for carbon co-deposits (a-C:H). Being an optical method it can scan large surface areas efficiently, but it also suffers from surface roughness and cannot identify the deposit composition, e.g. whether its ^{12}C or ^{13}C deposits. SIMS can probe very thick layers up to several 10 μm with isotopic sensitivity, but it cannot provide absolute deposition quantities and its accuracy suffers from surface roughness in the order of the layer thickness.

This work presents a new high throughput approach for acquiring improved quantitative deposition maps using nuclear reaction analysis with deuterons. Due to their physical nature, deuterons offer adequate reactions with most rare isotopes (^{15}N, ^{18}O…), but for practical reasons the method will be developed and described on the basis of ^{13}C analysis by deuterons. The new approach offers higher range and productivity compared to ^{3}He NRA, combining all the aforementioned individual strength' in one method. The application to two EAST tracer experiments will investigate this with first analytical outcomes. The same analysis will be conducted using the existing colour fringe and SIMS based analysis, where applicable. Finally, the quality of the new results will be discussed and compared to the alternative analysis method.

2. Experimental setup

Two methane (^{13}CD$_4$) injection experiments have been performed on EAST with D and He plasma, respectively. In each experiment, a 150x150 mm^2 tile of 25 mm thickness made from graphite is exposed. Each tile features 8 holes, a central 2 mm diameter hole for the methane (^{13}CD$_4$) injection, one for a Langmuir Probe, and 6 holes for mounting screws, see Fig. 1. These samples are assembled and exposed on the MAPES system [9,10] to the EAST plasma scrape-off layer (SOL) [11] in 9 consecutive shots each. The plasmas are designed for maximum reproducibility L-mode discharges in D and He with $P_{ECRH} = 0.8$ MW of electron cyclotron resonance heating power, 500 kA plasma current (I_P), and a flat-top line averaged density of 3×10^{19}/m^3. Correspondingly, the samples will be named D and He in the following. Fig. 2 shows the time traces of several consecutive discharges, demonstrating the high level of reproducibility of the EAST discharges. The methane injection rate is in the order of 10^{19} molecules/s during the flat-top phase, as indicated in Fig. 2. The comparison to a reference discharge without injection demonstrated only little impact of the injection on the core and
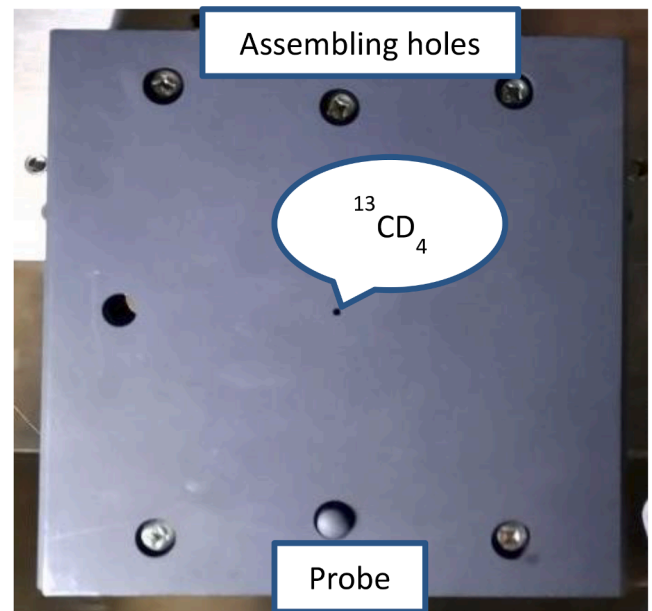

Fig. 1. Photography of the exposed graphite tiles as mounted.

local plasma parameters, but an indirect impact of the injection on the deposition process through a change in plasma properties cannot be excluded. Table 1 displays the sample exposure conditions. The values of the D and He experiments differ only slightly, with the D plasma resulting in a slightly higher local density and temperature according to the Langmuir probe on the sample. The sample position is at major plasma radius of R = 2335 mm, ~20 mm behind the last-closed flux surface. The main difference between D and He experiments is the reverse direction of toroidal magnetic field.

After exposure the sample are brought to Forschungzentrum Jülich for post-mortem analysis. Both He and D sample show visible colour fringes from thin deposited layers and a greyish shiny thick deposition zone around the central injection hole. Due to sample size limitations for post-mortem analysis, the tiles are sectioned to 9 equally sized blocks as depicted in Fig. 4. These blocks then go into surface analysis first by deuteron NRA, then SIMS and finally colour fringe analysis.

The NRA end-station provides a pressure of $8 \pm 2 \times 10^{-8}$ mbar during analysis. A 1.7 MV tandetron accelerator generates the 1430 keV deuteron beam with currents of 10–20 nA. For spot-size measurement, scintillating single crystals are placed on the sample holder and the spot-diameter is derived from the camera image to 0.2 ± 0.02 mm. The chamber features a 4-axis nano-manipulator with 10 nm resolution, a pA-meter (Keithley 6487) and a tele-centric observation camera with 20 μm resolution. Scanning works via a fixed beam position with a moving sample resulting in a constant detector geometry. The pA-meter measures the proton dose with a 120 V secondary electron suppression bias on the sample to 1% accuracy. A software integrates the current, yielding the collected charge. A 300 μm thick Si-detector is used for RBS and NRA. The RBS determined Particles × Sr values matches the current integration within uncertainties. This detector is used for all but the ^{13}C (d,p$_0$)^{14}C reaction, since the protons from this reaction cannot be fully stopped within 300 μm Si. A 1500 μm thick detector with a factor 12.8 ± 0.5 larger solid-angle and a 12.5 μm thick Kapton foil enables measuring the ^{13}C(d,p$_0$)^{14}C at increased count rates for better statistics at lower ^{13}C coverage. Both detectors sit on a 150° reaction angle.

The spectra are analysed via SimNRA 7.02 [12] with SRIM-2013 stopping powers. For data evaluation, cross-sections for ^{13}C(d, p/t/ α)^{14}C/^{12}C/^{11}B [13], ^{12}C(d, p$_0$)^{13}C [14] and D(d, p)^{3}He [15] are applied. A correction for outgassing of deuterium due to beam impact was not applied due to the short irradiation times of about 10 s and the dose of 0.2 μC per analysis spot. An automated mapping software distributes 30
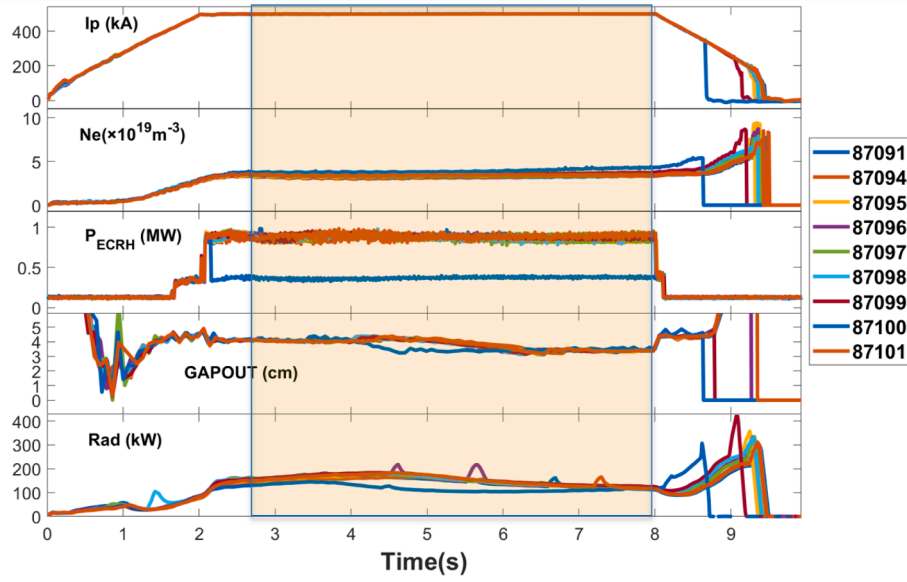
Fig. 2. Time traces of the plasma conditions of the injection experiments in EAST He-plasma. From top to the bottom: plasma current I_P, line-averaged electron density, heating power, outer gap between separatrix and limiter, core radiation. The highlighted frame marks the time-frame of $^{13}CD_4$ injection between 2.7 and 8 s after discharge start.

Table 1

Plasma exposure and injection experimental conditions. A reciprocating Langmuir probe measured the local plasma properties. The local values are taken at the same radial coordinate as the injection hole. The outer part of the sample is about 8 mm farther away from the last closed flux surface (LCFS) than the injection hole resulting in slightly lower n_e and T_e. The poloidal curvature of the plasma results in varying distances between sample surface and LCFS.

Experiment	Line-averaged Density [1/m³]	Pulses	I_P Flat-top [s]	Local N_e [1/m³]	Local T_e [eV]	Injected ^{13}C atoms	Injection [s]	Surface temperature
D plasma	3×10^{19}	9	54	4×10^{18}	22	7.49×10^{20}	47.7	~420 K
He plasma	3×10^{19}	9	54	3.4×10^{18}	22	7.91×10^{20}	47.7	~420 K

× 30 measurement points for the central blocks with the injection hole and 25 × 25 points for other blocks in a regular quadratic matrix over the accessible block surface area of about 46 mm edge length. This results in a lateral resolution of about 1.55 mm and 1.85 mm, respectively. This will prevent detection of fall-off length' shorter than 1.85 or 1.55 mm, respectively, which might occur close to the injection hole. In both experiments we will see ~10% of the deposited material rests within the central 25 points, corresponding to about 7 × 7 mm² or 2.2% of the sample surface. Even if this quantity is largely underestimated by

missing the highest point of the deposit thickness gradient, the impact on the total deposition efficiency would be rather small. Therefore, the systematic uncertainty induced by the limited lateral resolution will be neglected.

ToF-SIMS analysis is carried out using a 2 keV Cs sputtering beam on a 0.2 × 0.2 mm² area. Within this area a 30 keV Bi probing beam scans 44 × 44 μm². The ToF detector operates in negative ion mode. The sputtering stops upon changeover of ^{13}C dominated to ^{12}C dominated signal. A Dektak 6 m 1D profilometer with 12.5 μm tip at 15 mg force is

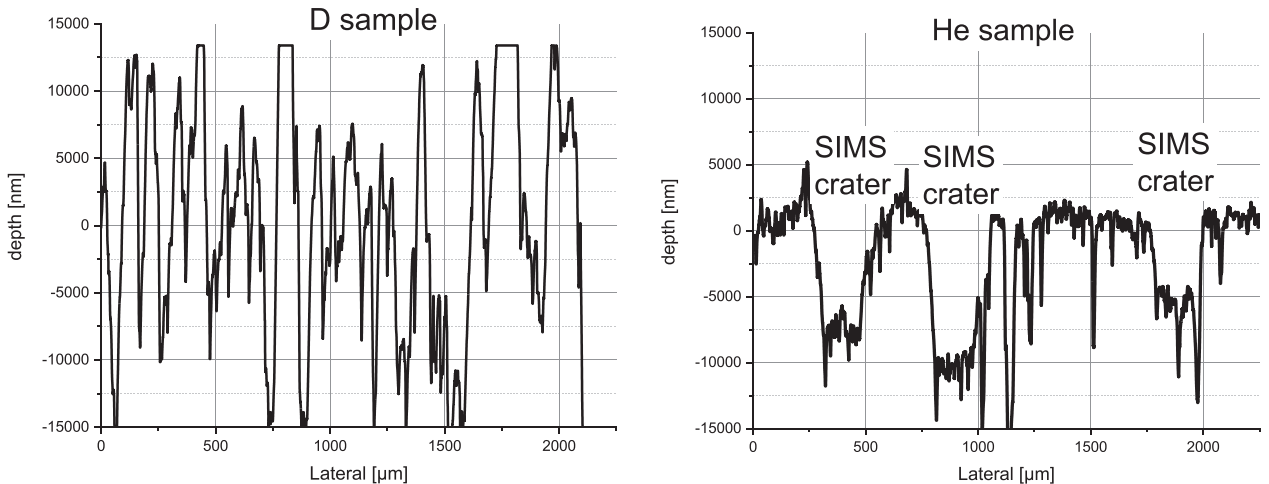**Fig. 3.** 1D surface profiles of both tiles. The D sample shows clearly higher roughness hiding the SIMS crater at x = 1500 μm, while the lower roughness of the He sample allows for measuring craters of at least a few μm depth.

used for SIMS crater depth measurement. This 1D profilometer determines a roughness value of $R_a = 1.07$ μm (He sample) and $R_a = 7.7$ μm (D sample) at 5 different lines of 3 mm length on the front surface, see Fig. 3. As the photos in Fig. 4 also show directed machining trenches dominate the surface roughness. For practical reasons the surface roughness is only analysed after exposure in EAST, but due to the lateral invariance of the R_a value, these values are assumed to be representative for the whole surface.

3. NRA method

The design of the analysis setup comprises three major questions regarding beam energy selection, radiation protection, and data analysis.

The nuclear cross-sections for all reactions with ^{13}C are available from [13] with an accuracy of 4.5% in a range of 0.5 to 1.7 MeV. The beam energy has to lie in this range to allow for a quantitative analysis. Fig. 5 shows the cross-sections in this range. Among these reactions the p_0 reaction offers the best range, while α_0 provides the best depth resolution and cross-section. All reaction cross-sections are relatively constant in a range between about 1.4 to 1 MeV. For technical reasons 1.43 MeV is selected. Higher energies would increase the maximum probed deposit thickness, but in particular the p_0 reaction cross-section would strongly drop, resulting in less constant signal intensity throughout the deposit thickness.

In the given setup, the protons of the $^{13}C(d,p_0)^{14}C$ reaction have about twice the energy of the $^{12}C(d,p_0)^{13}C$ protons and the α-particles from the $^{13}C(d, \alpha_0)^{11}B$ have about 500 keV higher energy than these. Together with the required high beam currents for mapping measurements this results in potential pile-up background, reducing the signal to noise ratio. While this contributes only 1–2% to the counts of thick ($\geq$μm) layers, the pile-up defines the detection limit for thin layers or low concentrations of ^{13}C. For layers thinner than the depth resolution both points become equal. Therefore, thick layer analysis profits from the higher range of $^{13}C(d,p_0)^{14}C$ and its large distance to other reaction peaks. For thin layers, a $^{13}C(d, \alpha_0)^{11}B$ based analysis offers higher count rate limits due to higher cross-sections and improved depth resolution of 2×10^{22} at/m^2, compared to 7×10^{22} at./m^2 for p_0 [16].

Fig. 6 demonstrates a measured spectrum of the thin detector for two extreme cases of deposit thicknesses. The spectra show the connection of
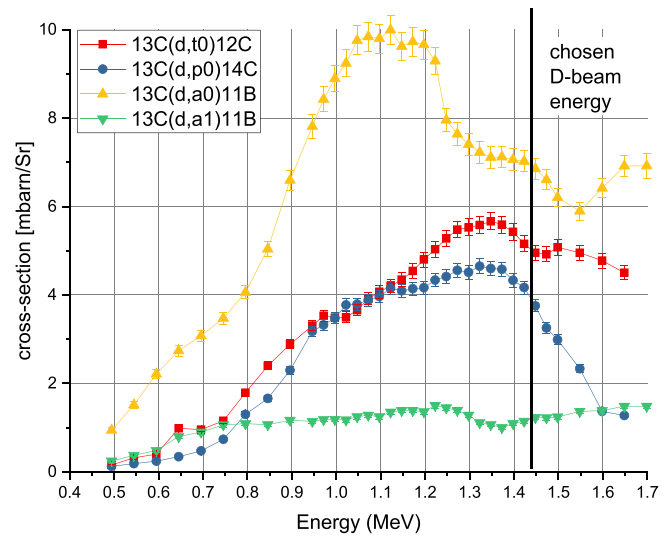

Fig. 5. The p_0 cross-section used for ^{13}C analysis shows a relatively flat region from 1 MeV to the applied deuteron energy of 1.43 MeV. The α_0 reaction has a flat part down to 1.2 MeV, but from there on it falls behind the large $^{12}C(d, p_0)^{13}C$ peak of the substrate. The flat regions justify linear calibrations between counts and ^{13}C content. Data from [13].

the $^{13}C(d, \alpha_0)^{11}B$ peak with the $^{12}C(d, p_0)^{13}C$ peak of the bulk above a certain layer thickness, limiting its use for thicker layers. The low energy tails of the NRA peaks, in particular for the thin layer case in Fig. 6, indicates the presence of a depth profile, roughness, or layer thickness variations. SimNRA7.02 [12] calculation suggests roughness alone cannot explain the low energy peak tails. Apparently a large thickness variation of the deposits in the order of the deposit thickness exists. Thick layer measurements show constant ^{13}C concentrations in the α_0 peak, favouring the explanation not by ^{13}C depth variations, but by lateral deposit thickness variations. Due to the relatively constant reaction cross-sections, this roughness changes the evaluation result <1% and will be neglected. SIMS also shows these profiles.

A complete SimNRA fitting analysis of all 3070 data-points acquired in this work would require specialised algorithms and high performance
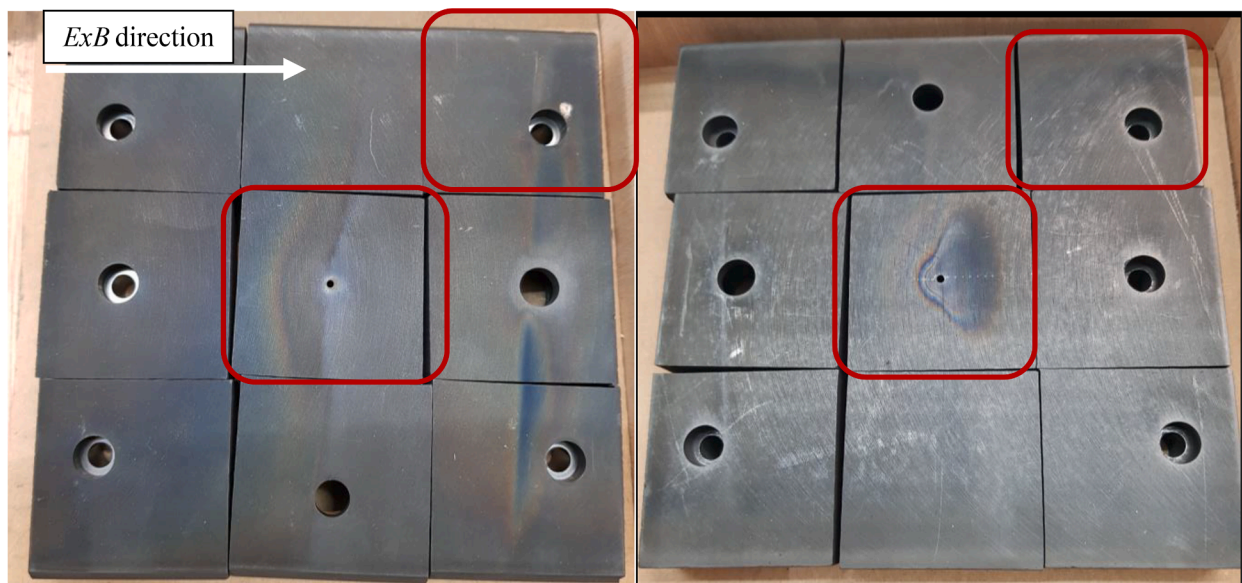

Fig. 4. Photos of the two EAST tiles sectioned into 9 blocks each. Left the D and right the He experiment tiles. Deposition patterns are clearly visible and mostly reproduced by the ^{13}C and D analysis below. In particular the patterns on the outer blocks probably relate to ^{12}C deposition. Two samples (red boxes) out of each tile are analysed in this work.
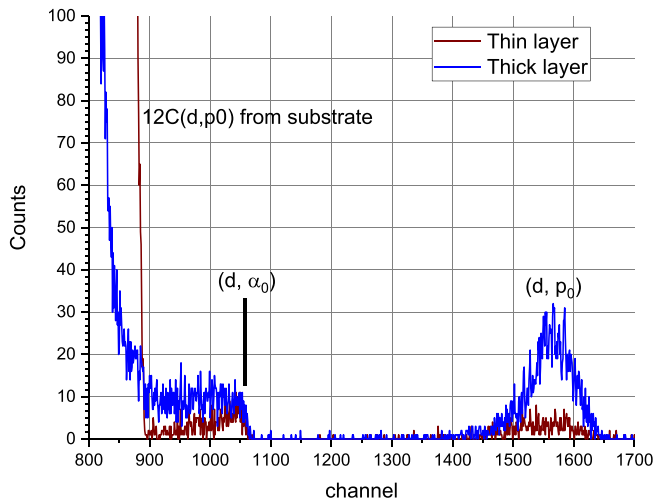
Fig. 6. Examples of thinner ($4.7*10^{22}$ D + C/m^2 ≈ 500 nm) and thicker ($1.2*10^{24}$ at/m^2 ≈ 12 µm) deposits measured by the 300 µm detector. The ^{13}C (d, α$_0$)^{11}B reaction clearly expands to the left with increasing deposit thickness, but remains at a count-level given by the ^{13}C concentration in the layer. This reaction sits near the high-energy flank of the ^{12}C(d, p$_0$)^{13}C reaction (the largest peak), limiting its use for thicker layers. Here the ^{13}C(d,p$_0$)^{14}C reaction adds range. The 300 µm thick detector was too thin for the full energy detection of the p$_0$ reaction, hence the peak form rather resemble a detector effect than the depth profile, but the integral counts connect linearly to the layer thickness.

computing, with questionable outcome due to the strong variation of layer properties over the sample surface. By fitting single spectra and simulating various deposit thicknesses based on the real fitted spectra, a connection between counts and ^{13}C and D content can be drawn for each individual reaction including variations of stopping power, cross-section, substrate ^{13}C, and pile-up. Fig. 7 demonstrates these connections to be linear, allowing a direct conversion of counts to deposit thickness with computing times of only a few seconds.

$$\frac{Counts}{\mu C} = 1653 + \frac{2.55}{\frac{10^{19} \ ^{13}C \ atoms}{m^2}} \tag{1}$$

Eq. (1) shows the acquired and normalised relation between NRA signal and deposited ^{13}C measured via the ^{13}C(d, p$_0$)^{14}C reaction as an example. Due to the isolated nature of the ^{13}C(d, p$_0$) peak, the flat depth profiles, and the relatively constant cross-sections between 1 and 1.43 MeV, we find linear connections. For the D(d, p)T reaction, the situation

complicates due to an overlap with the ^{12}C(d,p$_0$) reaction tail adding a significant background to the reaction. This results in increased uncertainties and worse detection limits, but due to the high D content in the co-deposits an analysis still yields credible results. The background was fitted by a 1st order polynomial and subtracted from the raw data prior to the analysis.

The irradiation of pure ^{13}C with deuterons produces 20 mBq of ^{14}C for 180 µC of integrated charge corresponding to 900 points irradiated for 0.2 µC each. German legislation allows for a release of up to 1 Bq/g of ^{14}C. Averaged over the ~100 g weight per block a total activity of 100 Bq would be acceptable. Correspondingly, the nuclear activation remains about three orders of magnitude below the critical limit, leaving enough room for increasing the point density and point dose. The beam-on radiation is more relevant for this analysis. The irradiation induces the ^{13}C(d, n)^{14}N reaction which has a cross-section of about 400 mbarn in the range of 1.2 to 5 MeV. The ^{12}C(d, n)^{13}N reaction features a cross-section of about 150 mbarn in this range, resulting in higher radiation levels for thicker ^{13}C deposits. Radiation levels require numerous changes and tight control of the beam optical settings for avoiding neutron emission from non-sample areas such as apertures and beam tubes. In this case sample radiation dominates the neutron dose levels, in particular for thickest deposits (most ^{13}C(d, n)^{14}N reactions). Here the neutron radiation represents the limiting factor for the beam current with 10 µSv/h @1 m distance reached with only 10 nA.

4. NRA results

Using this method in total four blocks are analysed, the central injection hole block and one diagonal block for each experiment, as marked in Fig. 4. The samples are aligned on a reference holder with 0.2° rotational alignment uncertainty. Fig. 8 and Fig. 9 show the results of the central block mapping. In both cases and for ^{13}C and D triangular deposition patterns with a maximum at the injection hole are visible. For the He sample the measured ^{13}C distribution resembles the optically visible deposition. For the D sample a correlation is more difficult since the area of thickest deposits appears grey-silverish, while the area of best visible fringe colours seems to contain only little ^{13}C. Within the accuracy, the NRA measurements yield >95% ^{13}C isotopic purity in the deposits, together with ~3% O impurities. It has to be noted that the method cannot detect ^{12}C layers. Integrating over the total block surface yields a deposition of $1.27 \pm 0.13 \times 10^{20}$ ^{13}C for the He and $1.78 \pm 0.18 \times 10^{20}$ ^{13}C for the D case. This corresponds to a deposition efficiency of $16 \pm 2\%$ in the He and $24 \pm 2\%$ in the D experiment. The D deposition accounts to $1.6 \pm 0.16 \times 10^{20}$ D in the He and $1.55 \pm 0.16 \times 10^{20}$ D in
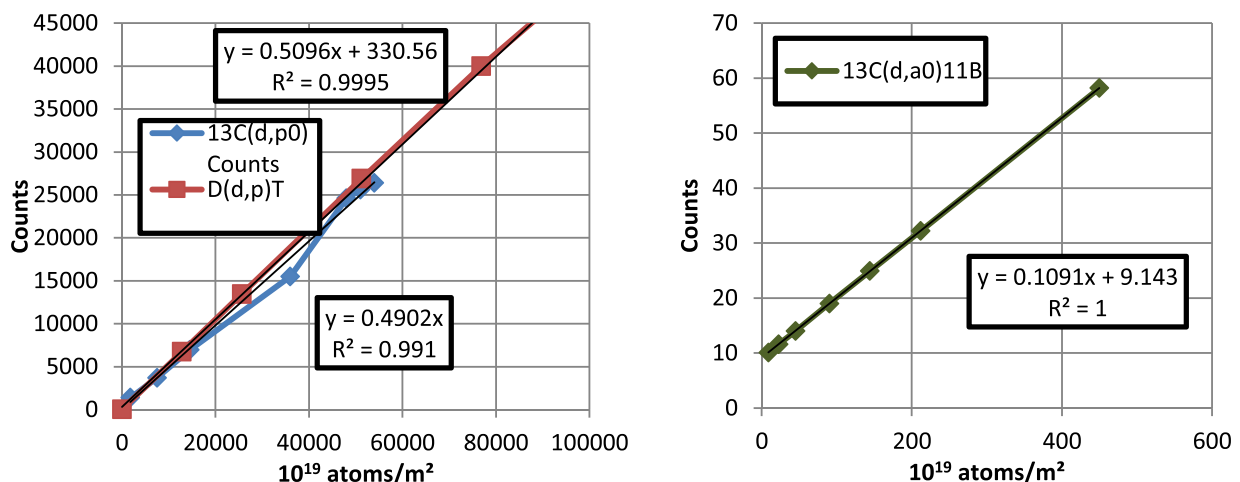

Fig. 7. Relations between SimNRA calculated region of interest counts and layer thickness for the given 0.2 µC of D ion dose per measurement point. In all three cases the relation between signal and layer thickness fits to a linear relation with R^2 > 0.99.
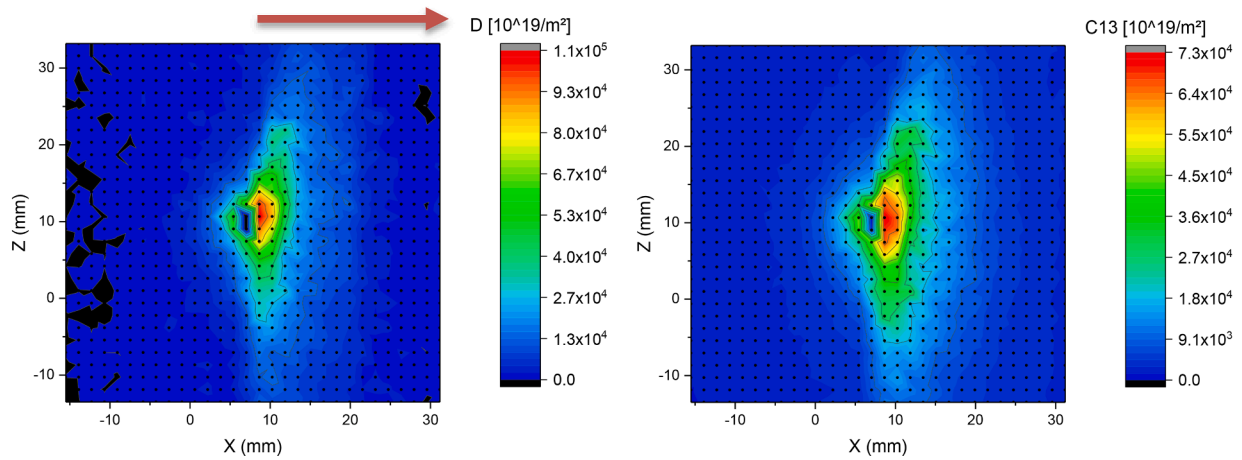
Fig. 8. Linear interpolation plots of the D and ^{13}C deposition on the central block of the D experiment. Black dots represent the NRA analysis points. D and ^{13}C patterns mostly agree to each other, indicating only slight variations in the D/^{13}C ratio of the layers. The red arrow indicates ExB drift direction.
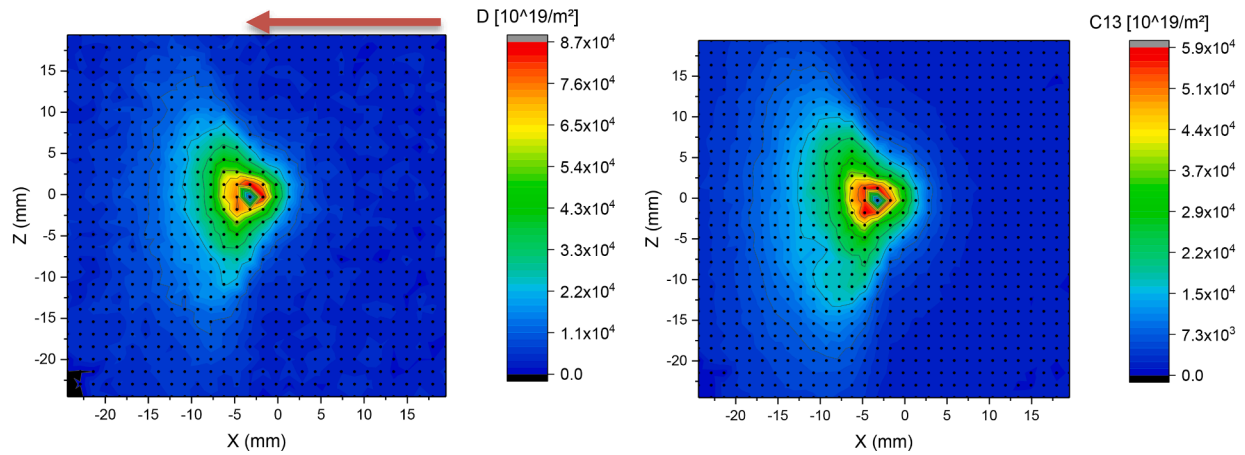

Fig. 9. Plots of the D and ^{13}C deposition on the central samples of the He experiment. In contrast to the D experiment the deposition is mirrored at the injection hole. The red arrow indicates ExB drift direction.

the D experiment.

In addition to the deposition efficiency and its lateral distribution, additional data can be extracted from the results. Fig. 10 investigates the a-C:D layer properties. The D/(D + C) ratio represents a central material quantity of these layers responsible also for its optical properties and its sputtering yields. For the D experiment, the results show a relatively constant value of 0.5, with slightly higher values close to the injection hole and smaller values outside the main deposition area. The He experiment resulted in slightly higher ratios. Here, even higher values appear on the right side of the plot (against ExB) and similar values as in the D experiment in the ExB direction.

The analysis of an additional outer tile aims at providing an estimate
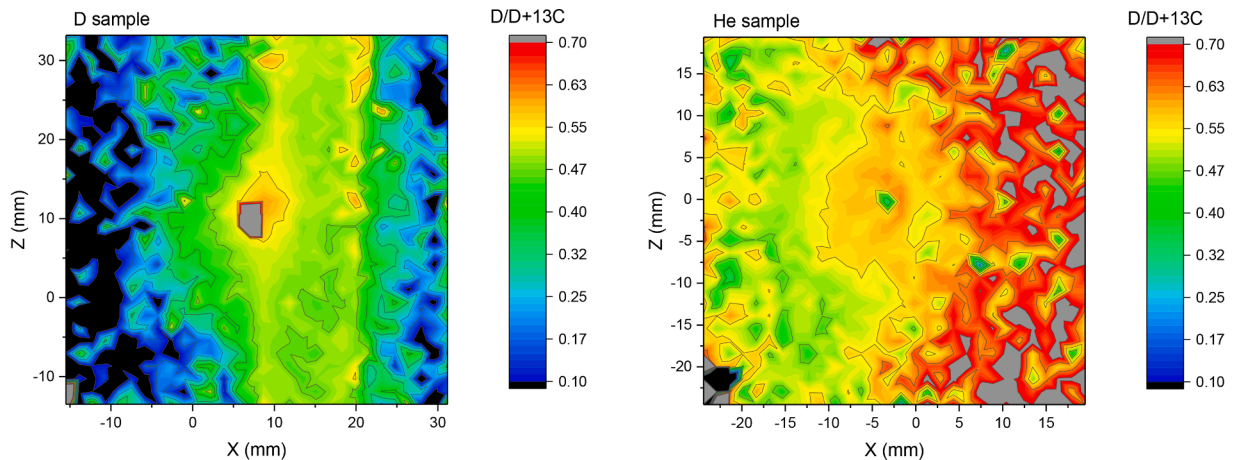

Fig. 10. Maps of the part of deuterium in the a-C:D deposits on the central sample (D left, He right). The outside regions are already dominated by noise/uncertainty.

for the long-range inventory and the radial distribution. For this purpose a 25×25 point grid is scanned on similar blocks of the He and D experiments, see Fig. 4. The dose of 0.2 µC of each point resulted in poor statistics of only a few 10 counts for the thin ^{13}C layers observed here, corresponding to only a few 10 nm of deposit. 4 counts of pile-up and 2 counts of background are subtracted from the $^{13}C(d,\alpha_0)^{14}C$ surface peak, resulting in an uncertainty in the order of 30%. Higher analysis doses or lower pile-up (lower ion beam current) would have improved the statistics, further reducing the detection limit. Here identical analysis conditions are chosen for practical reasons, yielding a detection limit of about 30 nm.

For the thin layers, the D amount cannot be determined from the D(d, p)^{3}He reaction, due to the large background from the $^{12}C(d,p_0)^{13}C$ peak. For SimNRA analysis, the D/C ratio is assumed to be consistent with the central sample, but the impact of the D content in the layer on the measured ^{13}C content remains small anyways. Fig. 11 displays the ^{13}C deposition results. Interestingly, the ^{13}C analysis does not resemble the colour fringe crossing the screw hole on these blocks, identifying these deposits as ^{12}C deposition. The samples show a total retention of 7.4×10^{17} ^{13}C (D experiment) and 3.2×10^{17} ^{13}C (He experiment). The D sample shows a radially symmetric behaviour (injection hole = origin) with equal vertical and horizontal exponential fall-off length of 9.9 ± 1 mm. The He sample in contrast has a slight asymmetry with a horizontal fall-off length of 7.3 ± 1 mm and a vertical of 5.3 ± 1 mm. A similar ^{13}C

exponential fall-off analysis on the central sample shows values of about 3 mm against ExB and 5–10 mm in ExB direction on both samples. In all radial lines drawn on any sample the offset exponential decay fit function describes the data with $R^2 > 0.9$, but quadratic and cubic polynomial fits also agree to the data.

This knowledge enables extrapolation of the total deposition on the exposed tiles. By assuming a radial symmetry, although not perfectly given as stated above, we can approximate all 8 outer sample to contain the same amount of ^{13}C resulting in $5.9 \pm 0.6 \times 10^{18}$ atoms (D sample) and $2.56 \pm 0.3 \times 10^{18}$ ^{13}C atoms (He sample), respectively. These numbers are about a factor 30 (D) to 50 (He) below the values of the central parts. In summary, the visible part of the fringe pattern around the injection hole contains ~80% of the deposit. The central blocks of 46×46 mm^2 contain ~98% of the deposited ^{13}C. The remaining 2% are located on the remaining 89% of the tile surface area. Integrating over the whole EAST tokamak could again yield in a relevant contribution, but requires complex modelling exceeding the frame of this work.

5. SIMS and colour fringe analysis results

The SIMS analysis of 6 points on the D and 16 points on the He sample reveals additional information and comparison of NRA to this established method. Fig. 12 shows an exemplary depth trace. The comparison of D and H signals yields H/D $\approx 0.14 \pm 0.02$ in both the He
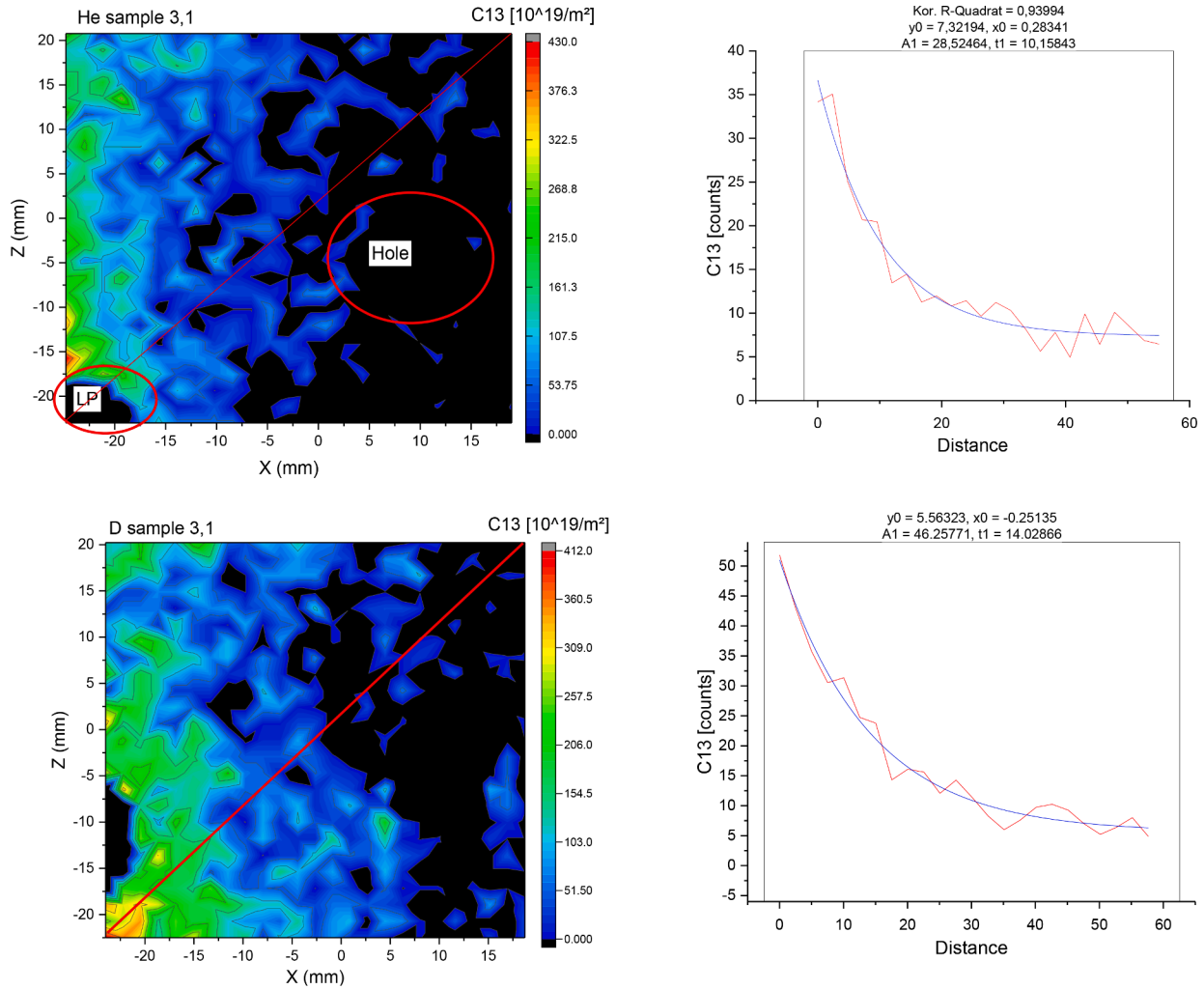

Fig. 11. The ^{13}C content of the upper-right He and D samples together with radial line plots. The ^{13}C surface layers are thin, but they show an exponential fall-off radially (red-line) from the injection hole starting at the bottom-left with a fall-off length of 10.1 mm (He) and 14 mm (D). The holes are the bores for fixing the tile. On the LP region on the bottom-left a scintillator was placed. The interference colour line visible in Fig. 4 seems to be uncorrelated to ^{13}C deposition.
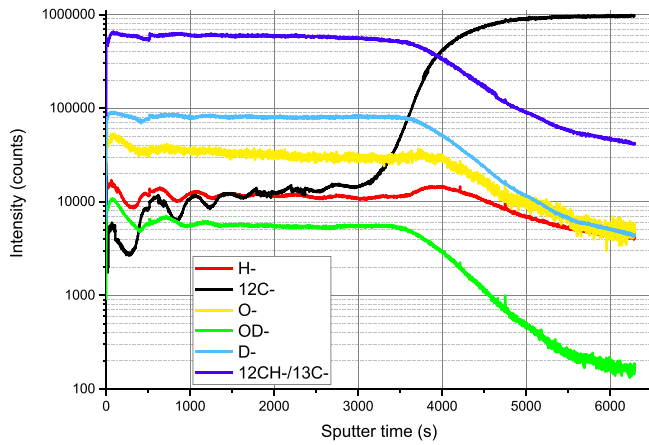
Fig. 12. Exemplary SIMS measurement of the co-deposit 2 mm right of the injection hole on the central He sample. The ^{12}C to ^{13}C isotopic ratio supports the NRA result indicating > 8% ^{13}C in the layer. The ^{12}C signal shows a periodicity probably related to the erosion flux variation during the 9 subsequent plasma discharges. The wide transition region starting at about 3000 sputterseconds relates to the surface roughness.

and D experiment. The measurement yields a ^{13}C isotopic purity of 98.1 ± 0.7% when comparing the mass 13 to the mass 12 signal. This number is clearly above the nominal 1% ^{12}C isotopic purity of the source gas, therefore ^{12}C either from the tiles themselves or the remaining vessel deposited on the samples. SIMS shows oscillations of the ^{12}C signal in the thicker layer parts, probably related to the plasma pulses which induce different ^{12}C erosion during ramp-up and ramp-down compared to the flat-top phase. The constant ^{13}C signal in these regions suggests variations in the ^{12}C erosion outside the sample, changing only this contribution to the deposition. The SIMS sputtering is stopped after completion of the transition from ^{13}C to ^{12}C signal. This allows for layer thickness measurement via profilometry. Due to the relatively long share of the transition region in the total sputtering time, the layer thickness derived from measured crater depth has a significant uncertainty.

In particular for the thick layers close to the injection hole, the SIMS measurements take up to 3 h per point. While the thinner layers require only a few 10 min of sputter time, the significant surface roughness results in a long transition region between layer and bulk, blurring the experimental result. The roughness of $R_a = 1.07$ μm (He sample) and $R_a = 7.7$ μm appears responsible for the smearing of the SIMS profiles near the substrate–layer interface. Deposit thicknesses below the roughness value can hardly be quantified. For the D sample this makes the whole SIMS analysis unusable.

Nevertheless, a few craters on the He sample can be analysed. One of the craters near the injection hole on the He sample yields a layer thickness of 8.5 ± 2 μm. Assuming a standard density of 1.7 g/cm^3 and D/(D + C) = 0.56, corresponding to 6.5 × 10^{28} ^{13}C/m^3 [17], this results in a SIMS measured deposit thickness of 5.5 ± 1.3 × 10^{23} ^{13}C/m^2. An NRA point within < 1 mm distance measures 5.4 ± 0.6 × 10^{23} ^{13}C/m^2, in agreement with SIMS. The next point 2 mm away from the hole with 6.4 ± 2 μm corresponding to 4.14 ± 1.3 × 10^{23} ^{13}C/m^2 compares well to 3.4 ± 0.4 × 10^{23} ^{13}C/m^2 measured by NRA.

Recalculating the measured amounts of D and ^{13}C together with measured SIMS crater depth allows calculating the layer density. Close to the injection hole layer densities from 0.75 ± 0.25 to 1.7 ± 0.25 g/cm^3 with D/(D + C) of 0.56 ± 0.06 are found in the He case for 5 SIMS craters placed up to 3 mm away from the injection hole. The values represent soft layers as expected from ~ 420 K sample temperature and the hydrogen rich injection gas [18], although the values are on the softest end of the observations. Comparing the calculated density to the standard assumption of 1.7 g/cm^3 equals a comparison of the deposit

thickness. Consequently not all point agree between SIMS and NRA. Probably the roughness and the corresponding uncertainty in SIMS crater drilling stop criterion tend an overestimation of the layer thickness in this measurement series due to too long sputtering times.

Visible colour fringes enable determining the layer thickness for known optical properties up to a deposit thickness of about 1 μm in the case of typical tokamak a-C:H layers [17,19]. For thicker layers, SIMS can provide information on layer thickness and composition. The comparison to SIMS craters sputtered in a colour fringe region, or the independent measurement of crater depth by a surface profiling method enables calibrating and correlating SIMS and colour fringe analysis. The colour fringe analysis and the photo Fig. 13 shows deposition patterns on the central He sample. The analysis of D tile suffers from the significantly higher roughness blurring the fringe colours to near invisibility. Only clearly visible fringe colours are used for the analysis. The applied fringe colours to layer thickness relation assumes a refractive index n = 1.6 of the layers and illumination by daylight.

By assuming standard optical properties of the layer, an optical model allows correlating the fringe colour and its order to a layer thickness range. The fringe analysis assumed a density of 6.5 × 10^{28} ^{13}C/m^3, corresponding to a density of 1.7 g/cm^3 with the above stated D/(D + C) = 0.56 (equal to the assumptions for SIMS analysis) as values typically resulting in n = 1.6. Measurement of the areal coverage of corresponding fringe colour results in a layer volume. The assumed layer density then enables calculating the ^{13}C deposition. Comparison of this deposition results in the region of visible colours on the He sample yields a value of 3 × 10^{19} ^{13}C using colour fringe analysis and 5 ± 0.8 × 10^{19} ^{13}C using NRA. The strong gradient in fringe colours induces larger uncertainties for this method in these experiments, hence numbers can be considered to roughly agree. Furthermore, the outermost parts of the deposits with thickness < 75 nm are not considered in the number above, since these thin layers do not result in a visible fringe colours, but
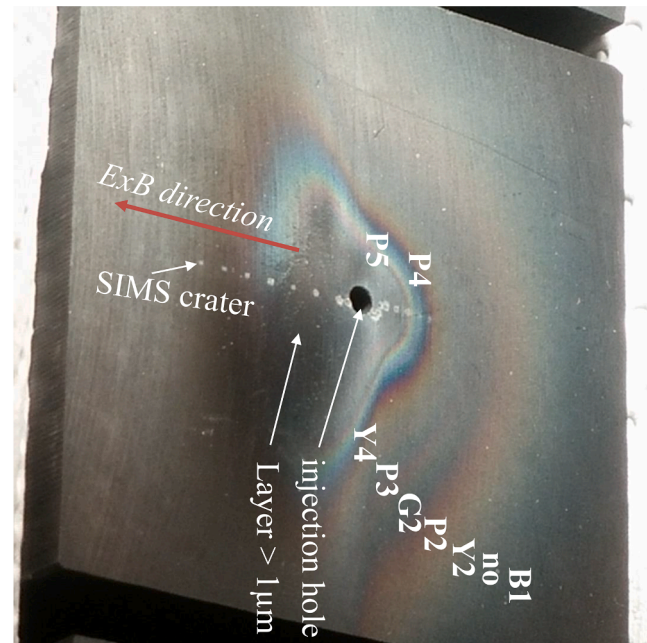

Fig. 13. Fringe colour analysis of the central He block with indicated colours and fringe order. Any regular interference order starts with yellow (Y) and passes purple (P), blue (B) and green (G) with increasing thickness, except the first which ends very pale (no) instead of green. Purple fringes are best visible and can be counted up to the sixth order. Not all fringes are indicated. First order yellow and purple don't appear, likely because of the rough surface. The black part contains the thick layer region with thicknesses >1 μm inaccessible by fringe analysis. The colours indicate increasing layer thickness towards the injection hole.

could contribute another 1×10^{19} ^{13}C. Compared to the total deposition of $1.27 \pm 0.13 \times 10^{20}$ ^{13}C, the colour fringe analysis detects only a small part of the total ^{13}C due to the large area of thick deposits close to the injection hole.

6. Methodical conclusions

For the first time we demonstrate the capabilities of high-throughput deuteron NRA for ^{13}C surface analysis at the example of a nuclear fusion tracer experiment. The method is developed by analysing the available nuclear reactions and their cross-sections, revealing about 1.43 MeV as an optimal beam energy. Radiation safety aspects, ^{14}C and neutron emission, are demonstrated to be acceptable. The method's speed allows for probing about 50–100 cm2 per day with a few thousand points. The absolute quantification with spatial resolutions down to 0.2 mm was demonstrated on about 100 cm2 of EAST plasma exposed sample surface area with 3070 data points. In the future these numbers can even be improved. A simplified data analysis based on calibration curves requires only a few minutes for evaluating the three investigated reactions on all measurement points. Using p and α reactions allows for good statistics in the range of 10^{20} to 10^{24} ^{13}C/m^2 for 10 s of measurement time per analysis point. The α reaction offers advantage for measuring thin layers down to a few 10 nm, while the p reaction offers the highest range enabling measurements of up to about 20 μm thick deposits. In comparison to SIMS, NRA required significantly shorter analysis times due to an inverse scaling of analysis time with layers thickness of both methods.

SIMS on the other hand offers better depth resolution, revealing in this case shot-wise fluctuations in the ^{12}C deposition flux and a more accurate quantity of the isotopic ^{13}C and hydrogen composition of the deposits. The surface roughness induces a minimum layer thickness in the order of the R_a roughness required for meaningful SIMS analysis and adds a systematic uncertainty regarding the stop-condition of the sputtering process. Finding and exactly implementing a stop criterion for the crater sputtering introduces additional systematic uncertainties into the SIMS results, generally resulting in an overestimation of layer thickness. Generally polished surfaces are recommended for any surface analysis, but deuteron NRA demonstrated a tolerance for roughness (here up to $R_a = 7.7$ μm) due to its analysis physics, making it suitable for technical surfaces.

Colour fringe analysis yields a rough agreement with the NRA data. The large probing area of colour fringe analysis makes it the fastest method. Its upper and lower limitations in analysed layer thickness of about 70–1000 nm are particularly problematic for the given experiments with their comparably thick deposits at the injection hole and thin deposits on the outer sample areas by preventing a full quantification of the deposition. In some places differences between NRA and colour fringe analysis revealed ^{12}C deposits on the sample. Since colour fringe analysis requires layer properties for a quantification of the deposition and the fringe colour is sensitive to surface roughness, both similar to SIMS, it experiences larger uncertainties compared to NRA which determines the relevant layer properties itself. The problem of varying layer properties (D/(D + C), density) and natural carbon deposits (^{12}C) from elsewhere in the device, as observed by the NRA analysis, represents a systematic weakness of colour fringe analysis and SIMS.

Deuteron NRA complements the set of tracer post-mortem analysis methods applied so far. The agreement with SIMS and colour fringe analysis supports its credibility. NRA as a quantitative method combines well with thickness measuring methods (SIMS, colour fringe analysis) resulting in the most complete analysis results of compositional, depth information, and layer properties. Generally, deuteron NRA is seen to offer the lowest uncertainties <10% and a suitable dynamic range regarding layer thickness and proves to be the most powerful method for deposition quantification. Deposits thicker than a few μm could only be probed by SIMS, so far. Due to a different thickness scaling deuteron NRA provides orders of magnitude higher productivity in this case.

Surface of technical roughness represent an additional uncertainty contribution to the alternative methods, but affects the deuteron NRA results only <10%, according to the literature. The decreased uncertainty and improved point density enable providing a 3D representation of the deposits for comparison with plasma-surface interaction models.

7. Physical conclusions

The NRA analysis found deposition efficiencies of $24 \pm 2\%$ (D) and $16 \pm 2\%$ (He) of the injected ^{13}C on the four analysed samples. The part of the total deposition in the optically visible layers close to the injection hole represents 80% of the estimated total deposition. Only about 2% of the ^{13}C are found farther away than 20 mm from the injection hole. Differences in deposition shape between D and He sample could be attributed to the plasma properties as the orientation of the deposition patterns follows the ExB direction. The similar plasma parameters, deposition efficiencies, and D/(D + C) in the He and D plasma indicate the deposition process being rather independent of the main core plasma species, but a sound assessment of the underlying physics/processes requires detailed modelling. This aspect cannot be covered in this work, but accompanying studies for plasma-surface interaction modelling and interpretation of the surface analysis results obtained here are ongoing to be published later.

The NRA measurements provide several additional information for such a modelling formerly inaccessible or not well-resolved enabling a deeper analysis of the underlying physical processes, most importantly spatial trends of the deposition efficiency and layer properties such as the hydrogen content. The following part offers possible interpretations of these observations, but the evidence only from surface analysis is too thin for a clear statement and requires further modelling and combination with other diagnostics. Layer properties and lateral distribution of thickness depend on the local plasma-surface interaction, therefore contain additional information on the deposited species and plasma edge conditions. Methane being volatile cannot deposit on surfaces at the low experimental surface temperatures of about 420 K [20]. It has to undergo an intermediate step, most probably a collisional reaction with electrons in the plasma close to the injection hole. In this case the deposition efficiency becomes independent of whether the injection is in a He or D plasma, only T_e and n_e matter. The relevance of the ExB drift (deposition triangle following ExB) for the deposition supports the assumption of at least a relevant intermediate ionised hydrocarbon step. The electron impact ionisation cross-sections of methane scales only weakly with plasma temperature for the observed T_e of both experiments [21], making variations of T_e negligible for the given situation. The triangular deposition shape possibly originates from the tile being flat, resulting in a minimum distance of the surface to the LCFS in the tile centre. This factor folds with a dilution of the injected methane with distance, resulting in the triangular shape as depicted in Fig. 14.

In all radial directions starting at the injection hole we see an exponential decrease of the deposit thickness. A pure geometrical reduction of the injected methane density with distance from the injection location would result in a quadratic to cubic behaviour which is incompatible with the observations. An exponential decay suggests a thinning of the depositing species by a reaction which depends on the depositing species density reducing it with distance from the source exponentially.

Since only 1/3 of the deposition follows the ExB direction (=2/3 in ExB half and 1/3 in other half), also a neutral (or radical or excited molecule) deposition channel must exist in parallel to the ion channel. A full breakup of the methane molecule appears improbable due to the many involved reaction steps, but the deposition of neutral CH_x with x < 4 is possible [20]. The deposition ratio of 1:2 of ionised to neutral (ExB independent) channel quite well reproduces the cross-section ratio of the reactions e + CH_4->e + H + CH_3 and e + CH_4->e + CH_4^+ at $T_e = 22$ eV [21], making them possible candidates for the relevant reaction step. Since electrons induce these reactions, D and He plasmas should result in
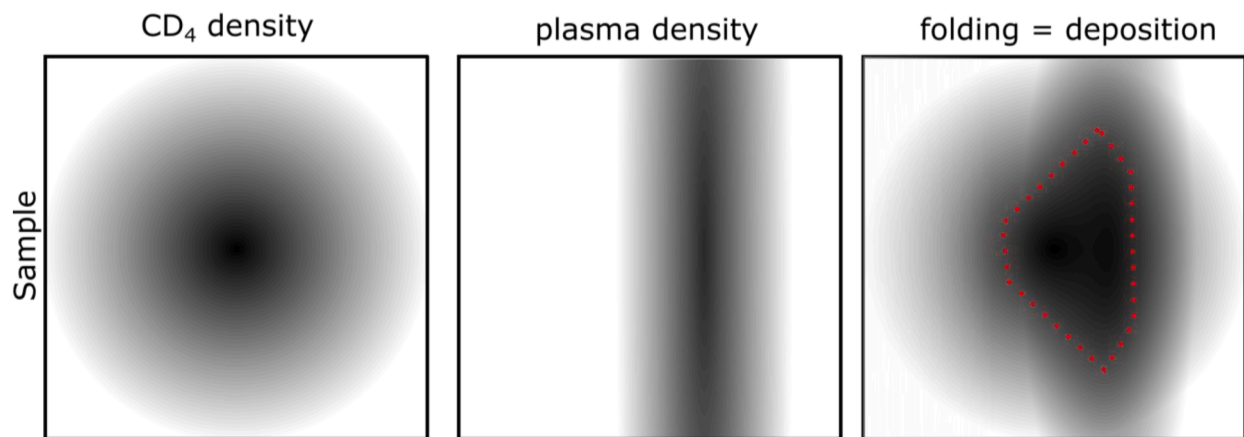
Fig. 14. Proposed origin of the deposition shape. Neutrals/Methane injected in the sample centre dilute geometrically (image shows linear gradient). A minimum distance between last closed flux surface and sample results in a maximum local n_e around the tile centre. Folding of both results in the highest deposition efficiency close to the injection hole in a triangular shape and a radial decay as shown in Fig. 8 and Fig. 9.

largely similar deposition patterns, only differing via ion induced sputtering. The CH_4 molecule cannot stick to a surface, but the CH_4 ion will be accelerated in the plasma sheath to about 100 eV and break up upon impact on the surface, allowing for a deposition [20]. Additional local spectroscopy would be required for a clear statement.

The D experiment shows a higher $D/(D + C)$ ratio in the ExB dominated deposition region suggesting a hydrocarbon with higher D/C ratio being responsible for the deposits in this region, since the more hydrogen atoms per molecule the higher the layer $D/(D + C)$ [18]. This supports the above assumption with the ion channel relying on a molecule with at least 1 more hydrogen atom than the neutral channel. In the He experiment the situation is not as clear since the detection limit of the D(d, p)T reaction and the subsequent noise level blur the image.

The $50 \pm 25\%$ higher local deposition efficiency of the D experiment can then be accounted to the 20% higher local n_e, the local T_e uncertainty could result in an increase of the above mentioned reaction cross-sections by 20%. The contribution of the 7.2 times higher R_a of the D plasma exposed samples could be in a similar order of magnitude with the given uncertainties. The results of [22] suggest a stronger scaling up to a proportionality of the deposition efficiency with R_a at least in the region of $R_a = 0.1$ to 1 μm (here 1.07 μm vs. 7.7 μm), but a dependency on plasma conditions was also observed there, limiting the transferability of those results. Consequently, the quantitative understanding of the impact of roughness is insufficient to state a (dis-)agreement with the observations made here and the origin of the higher deposition efficiency remains unclear.

The new results and the additional information on layer properties and spatial profiles together with the new accuracy of deposition provided by deuteron NRA could add important information for addressing the long existing question of enhanced re-erosion (ERE). Deuteron NRA provides unbiased results, due to its insensitivity to roughness, ^{12}C deposits, and a-C:H layer properties (density, D/C, thickness) compared to the SIMS and colour fringe analysis. The local variation of layer properties induces biased systematic uncertainties to any method based on interference colours and layer thickness. Uncertainties in NRA originate mostly from counting statistics. In conclusion, the new method extends the analysis capabilities to cases formerly considered difficult e.g. due to roughness or deposit thickness, but it could also provide different results for identical samples, compared to the other methods. The independence of the NRA result on surface roughness allows for more quantitative measurements of roughness impact on local deposition. The method could shed a new light on the ERE effect by providing known and significantly smaller statistical and systematic uncertainties. Systematic uncertainties in post-mortem analysis could have contributed significantly to the magnitude and necessity of the ERE effect due to its

weak impact on local net deposition efficiency. Lower uncertainties open up new testing grounds for origin and magnitude of the ERE.

CRediT authorship contribution statement

S. Möller: Software, Investigation, Visualization, Methodology, Formal analysis. **R. Ding:** Investigation, Methodology, Resources, Supervision. **H. Xie:** Formal analysis, Investigation, Visualization. **B.F. Gao:** Investigation. **B.G. Wang:** Investigation. **J. Peng:** Investigation. **S. C. Liu:** Investigation. **W. Gao:** Investigation. **A. Kirschner:** Resources. **U. Breuer:** Investigation. **P. Wienhold:** Investigation. **R. Krug:** Investigation. **S. Brezinsek:** Project administration.

Declaration of Competing Interest

The authors declare that they have no known competing financial interests or personal relationships that could have appeared to influence the work reported in this paper.

References

[1] P. Wienhold, et al., Investigation of carbon transport in the scrape-off layer of TEXTOR-94, J. Nucl. Mater. 290–293 (2001) 362–366, https://doi.org/10.1016/S0022-3115(00)00573-0.
[2] E. Vainonen-Ahlgren, et al., Studies on 13C deposition in ASDEX Upgrade, J. Nucl. Mater. 337–339 (2005) 55–59, https://doi.org/10.1016/j.jnucmat.2004.08.028.
[3] J. Likonen, et al., Deposition of 13C tracer in the JET MkII-HD divertor, Phys. Scr. T145 (2011), 014004, https://doi.org/10.1088/0031-8949/2011/T145/014004.
[4] S.L. Allen, et al., 13C transport studies in L-mode divertor plasmas on DIII-D, J. Nucl. Mater. 337–339 (2005) 30–34, https://doi.org/10.1016/j.jnucmat.2004.09.066.

[5] A. Kirschner, V. Philipps, J. Winter, U. Kögler, Simulation of the plasma-wall interaction in a tokamak with the Monte Carlo code ERO-TEXTOR, Nucl. Fusion 40 (5) (2000) 989–1001, https://doi.org/10.1088/0029-5515/40/5/311.

[6] A. Kirschner, P. Wienhold, V. Philipps, J.P. Coad, A. Huber, U. Samm, Modelling of carbon transport in fusion devices: evidence of enhanced re-erosion of in-situ re-deposited carbon, J. Nucl. Mater. 328 (1) (2004) 62–66, https://doi.org/10.1016/j.jnucmat.2004.03.011.

[7] R. Ding, et al., Modelling of local carbon deposition from methane and ethene injection through graphite and tungsten test limiters in TEXTOR, Plasma Phys. Control. Fusion 52 (4) (2010), 045005, https://doi.org/10.1088/0741-3335/52/4/045005.

[8] M. Mayer, Computer simulation of ion beam analysis of laterally inhomogeneous materials, Nucl. Instrum. Methods Phys. Res., Sect. B 371 (2016) 90–96, https://doi.org/10.1016/j.nimb.2015.11.032.

[9] 'Overview of plasma–material interaction experiments on EAST employing MAPES - ScienceDirect'. https://www.sciencedirect.com/science/article/pii/S0022311514006072 (accessed Mar. 23, 2020).

[10] R. Ding, et al., Material migration studies with an ITER first wall panel proxy on EAST, Nucl. Fusion 55 (2) (2015), 023013, https://doi.org/10.1088/0029-5515/55/2/023013.

[11] B.N. Wan, et al., Overview of EAST experiments on the development of high-performance steady-state scenario, Nucl. Fusion 57 (10) (2017), 102019, https://doi.org/10.1088/1741-4326/aa7861.

[12] M. Mayer, 'SIMNRA User's Guide', p. 67, 1997.

[13] J.L. Colaux, T. Thomé, G. Terwagne, Cross section measurements of the reactions induced by deuteron particles on 13C, Nucl. Instrum. Methods Phys. Res., Sect. B 254 (1) (2007) 25–29, https://doi.org/10.1016/j.nimb.2006.10.062.

[14] 'SigmaCalc recent development and present status of the evaluated cross-sections for IBA - ScienceDirect'. https://www.sciencedirect.com/science/article/abs/pii/S0168583X15008940?via%3Dihub (accessed Mar. 26, 2020).

[15] H.-S. Bosch, G.M. Hale, Improved formulas for fusion cross-sections and thermal reactivities, Nucl. Fusion 32 (4) (1992) 611–631, https://doi.org/10.1088/0029-5515/32/4/i07.

[16] M. Mayer, 'RESOLNRA User's Guide', p. 38, 2017.

[17] P. Wienhold, F. Weschenfelder, J. Winter, Colorimetry of interference colours to investigate thickness changes of protective coatings in TEXTOR, Nucl. Instrum. Methods Phys. Res., Sect. B 94 (4) (1994) 503–510, https://doi.org/10.1016/0168-583X(94)95428-3.

[18] T. Schwarz-Selinger, A. von Keudell, W. Jacob, Plasma chemical vapor deposition of hydrocarbon films: The influence of hydrocarbon source gas on the film properties, J. Appl. Phys. 86 (7) (1999) 3988–3996, https://doi.org/10.1063/1.371318.

[19] A. Kreter, et al., Study of local carbon transport on graphite, tungsten and molybdenum test limiters in TEXTOR by 13CH4 tracer injection, J. Nucl. Mater. 363–365 (2007) 179–183, https://doi.org/10.1016/j.jnucmat.2007.01.054.

[20] K. Tichmann, U. von Toussaint, W. Jacob, Determination of the sticking coefficient of energetic hydrocarbon molecules by molecular dynamics, J. Nucl. Mater. 420 (1) (2012) 291–296, https://doi.org/10.1016/j.jnucmat.2011.10.018.

[21] D. Reiter, 'The data file METHANE: Additional Atomic and Molecular Data for EIRENE', p. 89, Jan. 2020.

[22] A. Kreter, et al., Effect of surface roughness and substrate material on carbon erosion and deposition in the TEXTOR tokamak, Plasma Phys. Control. Fusion 50 (9) (2008), 095008, https://doi.org/10.1088/0741-3335/50/9/095008.